An *in situ* atomic force microscope for normal-incidence nanofocus X-ray experiments

M. V. Vitorino,[a,b]*‡ Y. Fuchs,[a]‡ T. Dane,[a] M. S. Rodrigues,[b] M. Rosenthal,[a] A. Panzarella,[a] P. Bernard,[a] O. Hignette,[a] L. Dupuy,[a] M. Burghammer[a] and L. Costa[a]

[a]ESRF – The European Synchrotron, 71 Avenue de Martyrs, 38000 Grenoble, France, and [b]Biosystems and Integrative Sciences Institute (BioISI), Faculdade de Ciências, Universidade de Lisboa, Campo Grande, 1749-016 Lisboa, Portugal. *Correspondence e-mail: mvvitorino@fc.ul.pt

Edited by V. Favre-Nicolin, CEA and Université Joseph Fourier, France

‡ These authors contributed equally to this work.

Supporting information: this article has supporting information at journals.iucr.org/s

A compact high-speed X-ray atomic force microscope has been developed for *in situ* use in normal-incidence X-ray experiments on synchrotron beamlines, allowing for simultaneous characterization of samples in direct space with nanometric lateral resolution while employing nanofocused X-ray beams. In the present work the instrument is used to observe radiation damage effects produced by an intense X-ray nanobeam on a semiconducting organic thin film. The formation of micrometric holes induced by the beam occurring on a timescale of seconds is characterized.

1. Introduction

High-brilliance third-generation synchrotron radiation sources have permitted the investigation of the structure of matter across a huge range of scientific disciplines. More recently, the development of high-flux focused X-ray beams (from tens to a few hundreds of nanometers) has allowed such experiments to be performed with high real-space resolution, permitting the characterization of local variations in structure. Despite such advances, the acquired data represent a structural average over hundreds to millions of atoms and molecules.

With the ever-increasing brilliance of synchrotron radiation sources, the high flux density of focused X-ray beams ($\sim 10^{10}$ photons s^{-1} in 100 nm $\times$ 100 nm area) has meant that radiation-induced damage of samples has become a significant problem in determining accurate structural information. Such damage is particularly significant for biological and soft materials (Alizadeh *et al.*, 2015). Furthermore, this damage has fundamental relevance in biomedical research (Brenner *et al.*, 2003). It has been reported that damage to materials can begin before any change is observed in the diffraction patterns, thus making such phenomena difficult to quantify by X-ray methods alone (Garman, 2010).

A number of approaches have been proposed to understand and reduce the effects of beam-induced radiation damage. Crystallographic data have been correlated with other microscopy techniques including *in situ* and *ex situ* scanning transmission X-ray microscopy (Smit *et al.*, 2008), scanning near-field optical microscopy (Larcheri *et al.*, 2008) and scanning tunneling microscopy (Gimzewski *et al.*, 1992). Adaptation of atomic force microscopes (AFMs) for use on synchrotron beamlines provides a promising approach to characterize beam damage. Besides achieving single-molecule resolution, AFMs offer the possibility to explore mechanical,
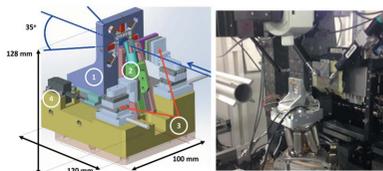
conductive and magnetic properties of materials (Rodrigues *et al.*, 2008, 2009; Schmid *et al.*, 2010; Pilet *et al.*, 2012; Slobodskyy *et al.*, 2015). Rodrigues *et al.* have investigated the Young's modulus of SiGe islands combined with X-ray diffraction, using the AFM probe as a nano-indenter, applying force to the materials on the nanoscale. Schmid *et al.* and Pilet *et al.* have combined X-ray microscopy and AFM with specially fabricated tips, in a normal-incidence configuration, to access the chemical and physical properties of polymer blends, lithographic metal structures and magnetic thin films. Meanwhile, Pilet *et al.* (2012) and Ren *et al.* (2014) have used nanofocused X-ray beams in combination with an AFM to study the mechanical deformation of Au islands.

Whilst these studies have demonstrated the utility of the AFM to induce nanoscale structural changes through applied forces, improving the temporal and spatial resolution of X-ray and AFM coupled experiments remains a central goal. Improvement in the incidence flux of X-ray beams and modern detector technology has enabled the observation of processes at the microsecond timescale. In conventional AFM, the acquisition of a single image can take up to several minutes, thus there is a significant gap to bridge when combining these instruments. The recent development of the high-speed AFM (HS-AFM) technique has improved the scan rate, permitting dynamic investigations into biological and soft matter systems (Ando *et al.*, 2014). Combining HS-AFM with scanning nanobeam X-ray experiments to rapidly yield simultaneous morphological and structural information is therefore an attractive goal. Finally, a significant challenge when working with scanning X-ray nano diffraction is the pre-alignment of the samples into the X-ray focal plane and the selection of regions of interest, which is typically done using an optical microscope. In cases where the sample features are too small to be observed by optical methods, an *in situ* AFM would facilitate the localization of samples.

To study biological material under physiological conditions, we have recently developed an X-AFM capable of observing the effects of radiation damage and performing AFM coupled to X-ray reflectivity on hydrated biological samples (Gumí-Audenis *et al.*, 2015). In this work, we extend the concept of an *in situ* synchrotron X-AFM to the normal-incidence geometry. We have developed an HS X-AFM capable of performing high-speed imaging (3.3 images s^{-1}) of the nanoscale morphology of soft matter systems, compatible with nanofocus synchrotron beamlines. Certain X-ray focusing systems require a very short distance between the last optical element and the X-ray focal point (as little as a few millimeters), which imposes significant constraints on the design of the AFM. The instrument has been specifically designed to be compatible with the nanofocus endstation of beamline ID13 at ESRF, the European Synchrotron. Despite this, it is adaptable to almost all normal-incidence beamlines in synchrotron radiation facilities, due to its compact design.

In this work, we explore the instrument capabilities to provide *in situ* nanolocalization of the nanobeam and, as a proof-of-principle experiment, we address the problem of localized radiation damage, correlating the effects observed both in the two-dimensional (2D) XRD pattern and in the AFM images. The test samples are drop-cast thin films of a thiophene-based pi-conjugated oligomer abbreviated hereafter as 4ThDiC8 (see *Experimental* section for more details). Such organic molecular semiconductors are promising functional soft-matter-based systems for low cost, solution-processable electronic and optoelectronic devices such as LEDs, lasers, FETs and solar cells (Forrest, 2004). We show that the instrument can detect morphological changes of the oligomer film's structure due to X-ray irradiation-induced damage, occurring on a timescale of seconds.

The HS X-AFM allows high temporal resolution and the possibility to acquire *in situ*, in normal-incidence configuration, both AFM and small- and wide-angle X-ray scattering (SAXS and WAXS) data.

2. Instrument description

The instrument is a sample-scanning AFM, meaning that the tip stays fixed (once aligned with the X-ray beam), whereas the sample stage is incorporated into an assembly that relies on fast piezoactuators to achieve high scan rates. Fast imaging of soft matter also depends on small and soft cantilevers with a high resonance frequency, and a focused laser detection methodology. A fiber-optic-based interferometer is employed to measure the AFM cantilever position and oscillation amplitude in contact mode and amplitude-modulation mode, respectively (Martin *et al.*, 2002). The HS X-AFM follows the same basal commissioning guidelines already detailed for a custom AFM for a synchrotron grazing-incidence beamline by Gumí-Audenis *et al.* (2015). The reader is referred to Ando *et al.* (2014) as well as to Fantner *et al.* (2006) for details on the construction of a HS-AFM. In this instrumental section we focus only on the key aspects of the adaptation of this instrument to the normal-incidence configuration in a synchrotron radiation beamline.

2.1. AFM overview and general features

The HS X-AFM weighs 1.83 kg and has a compact design, featuring a thickness along the beam direction, at beam height, of 21.25 mm and a height of 128 mm. The base of the AFM was designed such that it is easily adaptable to any sample holder. Among the instrumental design considerations for the HS X-AFM are the geometrical constraints necessary to achieve clean nanofocused X-ray beams. Fig. 1(*a*) presents a design of the microscope. Unlike any other conventional AFM, the sample is mounted perpendicular to the AFM base to allow for normal-incidence transmission X-ray scattering experiments. The sample is mounted in the center of the instrument, with the cantilever and detection system located upstream (towards the beam source). To allow for the transmission of scattered X-ray photons, no further instrumentation is positioned downstream of the sample. An open cone with half-angle 35° is built into the holder. Thus, when mounted on suitably transparent substrates (*e.g.* silicon nitride membranes), this design permits the acquisition of 2D SAXS
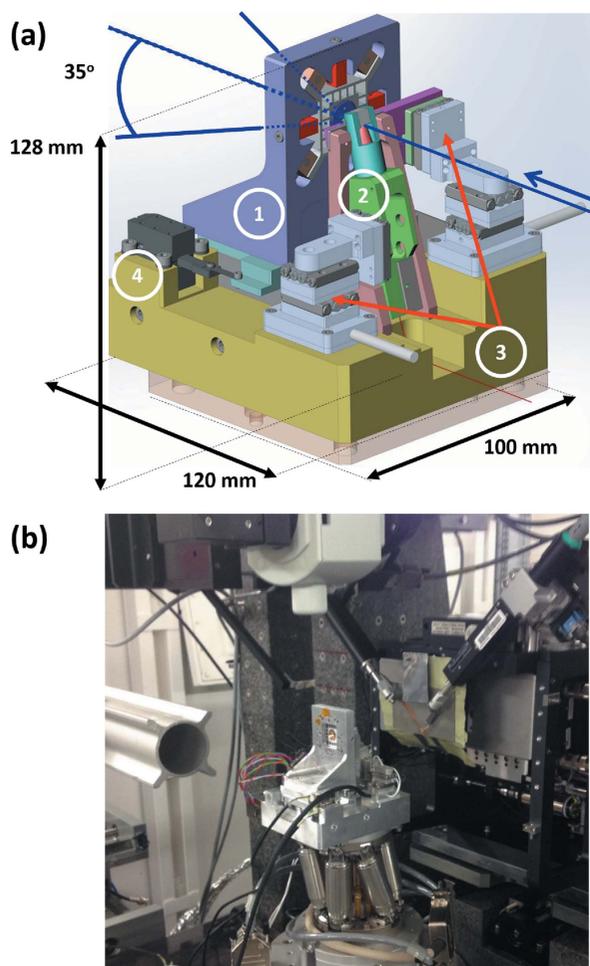
Figure 1
(*a*) Configuration of the normal-incidence HS X-AFM. The path of the X-ray beam is shown in dark blue. The sample is mounted upstream of the scanner (1). The cantilever and measurement system (2) are located upstream of the sample. (3) and (4) represent the alignment and long-range approach motors, respectively. The beam exits the scanner with a maximum half-angle of 35°. (*b*) HS X-AFM mounted in the nano hutch of ID13.

and WAXS (up to a diffraction angle of $2\theta = 35°$) data without shadowing by the AFM cantilever or holder. This is different in comparison with the instrument described by Pilet *et al.*, in which a downstream AFM tip was used as the primary X-ray detector (Pilet *et al.*, 2012). In our case we do not employ the tip as X-ray detector but our setup allows the acquisition of diffraction data. To prevent significant attenuation or modification of the incoming X-ray beam, we used either extremely thin (200 nm) cantilevers or probes that protrude from the end of the cantilever. Besides the basic instrumentation necessary to perform an AFM experiment, we have included in the cantilever holder the possibility to fit two other apertures on the AFM itself: the first one is used when the AFM is not in operation (aperture 1), whereas the second one is used when performing AFM measurements (aperture 2). They can be employed to reduce background scattering, to improve small-angle resolution or to serve as an order-sorting aperture (OSA) when using Fresnel zone plates to focus the beam. These two assemblies are aligned with the same sub-nano-meter positioning system that is employed in the cantilever alignment with both the laser and X-ray beams. Aperture 1 can be placed in the X-ray beam path from contact until 3 mm upstream of the sample, whereas aperture 2 is fixed at 7 mm from the sample. As such, the HS X-AFM serves not only to combine the two instruments but also as a sample holder capable of localizing the beam within the sample with nanometric precision.

To perform a coarse pre-alignment of the AFM tip to the X-ray beam position, a combination of the AFM inertial motors (items 3 and 4 in Fig. 1) and a hexapod (in our case ID13's) is used. Fig. 1(*b*) shows the instrument mounted on the coarse positioning hexapod [H-810, Physik Instrumente (PI) GmbH & Co. KG] on beamline ID13 of the ESRF.

2.2. Scanner

The scanner performs the fast rastering movement of the sample and the nano-alignment of the tip and the beam with the desired sample region. Fig. 2 presents the design of the scanner. We followed a philosophy introduced by Fantner *et al.* (2006), in which the in-plane movement of the sample is performed by two piezoactuators for each direction. These are tightly fixed between a system of flexure hinges that ensures the rigidity (high resonant frequencies) and at the same time minimizes the recoil of the supporting structure and the orthogonal in-plane displacements with respect to the direction of actuation. In order to perform the movement along the direction of the X-ray beam, a ring-shaped piezoactuator is fixed in the center of this assembly. The ratio between the inner radius and the thickness of this piezoactuator ultimately defines the half-angle of the free scattering cone (35°). The sample is attached to this piezoactuator through a magnetic ring. The maximum scan rate achieved with the HS X-AFM is 3.3 images s^{-1} (128 pixels × 64 lines), limited solely by our electronic control module, *SPECS Nanonis*. The maximum scan size is 3.6 µm × 3.6 µm × 1.0 µm. We have built a second scanner that permits a larger scan area (16.1 µm × 19.3 µm ×
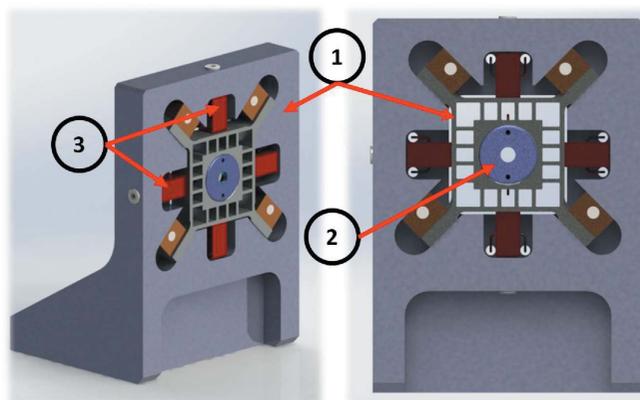
Figure 2
Scanner design for the HS X-AFM. The main components of the piece are indicated, including the outer/inner frames (1), the magnetic sample stage (2), behind which is placed the vertical piezoactuator, and the lateral piezoactuators (3).

2.3 μm) with lower speed imaging rates (0.3 images s^{-1}). We present a high-speed movie (see movie 1 of the supporting information; 3.3 images s^{-1}) obtained *ex situ* with the fast scanner on a silicon sample calibration grating in the third section of the supporting information.

2.3. Detection scheme

In addition to the use of very small probes (usually tens of micrometers long, 2 μm wide and 0.2 μm thick), fast imaging requires highly focused laser beam detection schemes in order to illuminate solely the small back-side of the cantilever avoiding spurious reflection from the sample surface. Fig. 3 presents a scheme of this detection assembly. Unlike conventional AFM, we have adapted an interferometric detection scheme (Rugar *et al.*, 1989; Hoogenboom *et al.*, 2008; Costa *et al.*, 2014; Vitorino *et al.*, 2015) due to the spatial constraints of the instrument. This detection methodology offers very high signal-to-noise ratio (Hoogenboom *et al.*, 2008). The interferometric system is adapted from the one previously reported by Gumí-Audenis *et al.* (2015). Here, the laser beam outputs from an optical fiber (5 μm core) located approximately 50 mm far from the cantilever. It is then collimated, refocused and directed to the cantilever back-side through a series of lenses and a mirror. It is reflected on the cantilever back-side and coupled back to the fiber. The interference between the laser beam reflected at the fiber end and the beam reflected at the cantilever back-side allows for the precise measurement of the AFM tip position.

3. Experimental

An X-ray beam of energy E = 19 keV (wavelength λ = 0.6525 Å) was focused to a beam size of approximately 250 nm
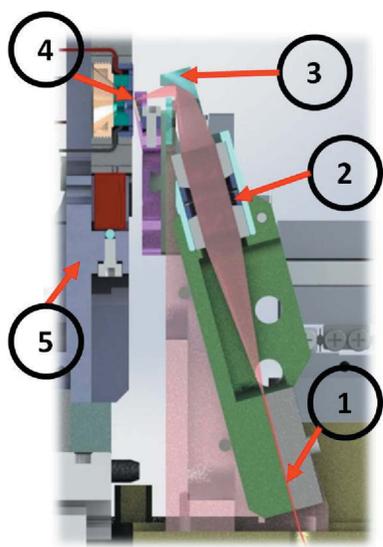
Figure 3
Cross section of the optical detection scheme design for the HS X-AFM. The main components are indicated, including the optical fiber (1), the laser beam collimator/focusing scheme (2) and the mirror (3). Also indicated are the AFM tip (4) and the scanner (5).

× 250 nm by Fresnel zone plates, with a recorded flux of 3×10^8 photons s^{-1}. Higher orders of the focused X-ray beam were removed by an order-separation aperture (an additional aperture from the beamline, not installed in the X-AFM). X-ray diffraction patterns were collected on an EIGER 4M detector (DECTRIS Ltd, Switzerland) with 2070 × 2167 pixels (horizontal × vertical) and pixel size of 75 μm × 75 μm.

The test sample, 4ThDiC8, is a thiophene-based organic semiconductor consisting of a quaterthienyl optoelectronically active core, end-capped by two *n*-octyl solubilizing moieties (5, 5′′′-dioctyl-2,2′:5′, 2′′:5′′, 2′′′-quaterthiophene; chemical formula: $C_{32}H_{42}S_4$; CAS number: 882659-01-0). 4ThDiC8 was synthesized, chemically characterized and provided by Dr Patrice Rannou [Structures and Properties of Molecular Architectures Laboratory, UMR5189-SPrAM (CEA/CNRS/UJF), Grenoble, France]. A 1 mg ml^{-1} solution of 4ThDiC8 in toluene was prepared. 5 μl droplets of the solution were deposited on silicon nitride (Si_3N_4) membranes (membrane window area 5 mm × 5 mm, membrane thickness 200 nm or 1 μm) (Silson Ltd, Northampton, UK) and left to evaporate in air. When dried, the resulting films consisted of micrometer-sized crystals of 4ThDiC8. We used ATEC-NC cantilevers, purchased from Nanosensors, in these experiments. Despite being relatively thick (4 μm), this probe features a tip protruding from the cantilever at an angle of 45–60°, allowing for the disentanglement of the absorption signal of cantilever and tip, thus making the alignment easier.

4. Results and discussion

At first we report the X-ray–AFM tip alignment procedures developed at ID13. Then, we investigate localized radiation damage effects occurring when the beam hits just one region of the sample in the absence of AFM scan during exposure. In this static experiment, the damage was characterized both by AFM and X-ray diffraction at timescales of seconds and minutes. Finally, we irradiated the sample while performing AFM in a dynamic experiment. In this configuration we did not observe any damage occurring up to an exposure time of 25 ms.

4.1. AFM tip–nanobeam alignment

We first show how the tip can be located with the beam. The modular character of this instrument permits the removal of certain components from the beam path. The first stages of alignment were performed with the scanner and sample removed from the AFM. Using the ID13 optical microscope positioned downstream of the AFM, it was possible to localize the cantilever to 1 μm precision [Fig. 4(*a*)]. To align the tip with the X-ray beam with more precision, the optical microscope was removed and the cantilever (together with the entire AFM) was raster scanned using the hexapod, measuring the absorption profile with a photodiode. To prevent beam damage to the sample during alignment, this step was first performed with the scanner and sample removed, then with the scanner and sample attached on a portion of the sample

research papers
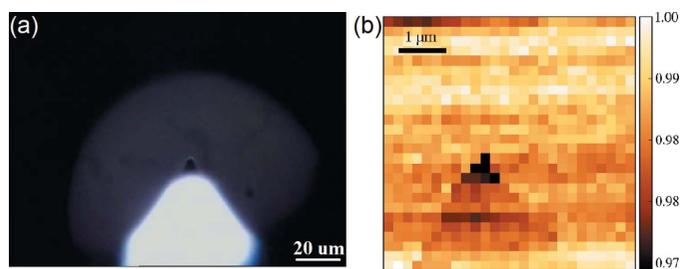
Figure 4
(a) Optical image of the AFM tip. This image is employed for the coarse alignment between the X-ray beam and the tip. (b) Scanning transmission X-ray microscopy showing the AFM tip in a scan approximately 20 times smaller than the image presented in (a). This measurement is used for the fine alignment between tip and X-ray beam.

away from the region of interest. The 2D raster scanning absorption map shown in Fig. 4(b) demonstrates that the tip can be aligned to the X-ray beam to an accuracy of 200 nm (i.e. smaller than the beam size). The inclined silicon probe of the ATEC-NC cantilever gave a maximum absorption of about 2% of the incoming intensity in the thicker region of the tip.

We did not succeed in aligning the X-ray beam and AFM tip by measuring the current, due to the charges photoemitted from the cantilever once the X-ray beam was incident on it, as we described in the alignment procedures of another X-AFM

(Gumí-Audenis *et al.*, 2015). We think this is due to the lower flux employed in this experimental session, causing lower signal-to-noise ratio.

4.2. Localized radiation damage

To explore the effect of localized radiation damage, we first performed an experiment whereby the sample was repeatedly exposed to the X-ray beam at a fixed position. AFM images were acquired between each X-ray exposure (i.e. in the 'dark') to monitor the morphological effect of the X-ray beam on the sample. For the purpose of this initial test, we used the slower, longer-ranged, scanner such that we could obtain a larger field of view (the reader is referred to Fig. S2 in the supporting information for *in situ* high-speed images of the same sample acquired at 1 image s^{-1}). AFM images acquired prior to X-ray exposure [Fig. 5(a)] show distinguishable plateaux of about 600 nm in height, which can extend for several micrometers. The sample was then exposed to the X-ray beam for 10 min (with the AFM scanner off) at the position indicated by the red dot in the AFM image in Fig. 5(a). Whilst there was no significant change to the morphology at the exposure position, a region located less than 1 μm [cf. blue dot in Fig. 5(b)] away showed significant degradation, as shown in the inset of Fig. 5(b). This damage manifested as a hole of depth 150 nm in
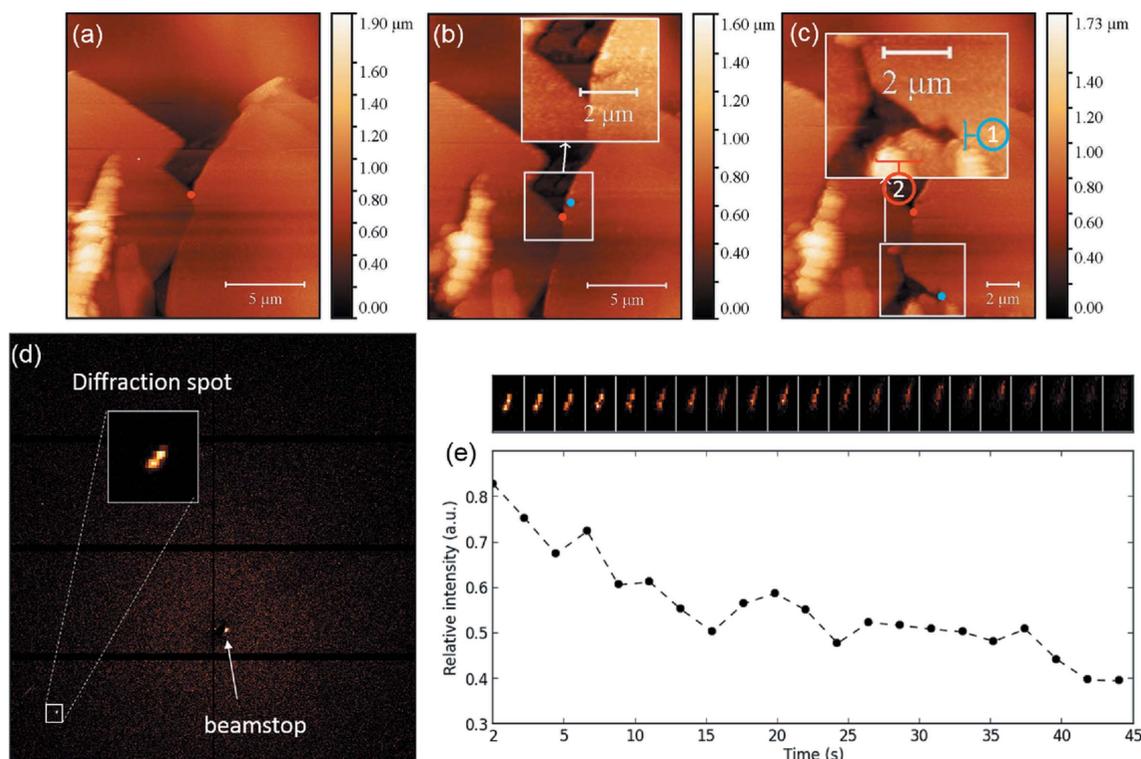
Figure 5
Localized radiation damage effects observed by AFM and XRD. (a) AFM image before exposure to X-rays. (b) AFM image after 10 min of exposure. We observe a 150 nm deep hole which is shown in a zoom (inset). The red spot shows the tip location during the illumination. The light blue spot shows the beam location during illumination. (c) AFM image after a 10 min exposure in an area located 4 μm below the area previously exposed (blue spot). An additional hole is observed (zoom in the inset) where we can distinguish the beam footprint [vertical and horizontal tails in the zone denoted by (1)] as well as a horizontal more pronounced damage extended over 5 μm (2) and large aggregates below the beam position. (d) Section of the 2D XRD pattern showing the beamstop and diffraction spot. (e) Sum intensity of the diffraction feature as a function of time. Inset, on top: sequence of the highlighted diffraction feature after repeated exposures to the X-ray beam.

the plateau. We note that a small error is expected in the relative positioning between the tip and sample due to creep and hysteresis of the piezoelectric actuators.

A second 10 min exposure was then performed, with the beam positioned 4 μm below the previous exposure [*cf.* blue dot in Fig. 5(*c*)]. The AFM image acquired afterwards reveals more significant morphological change [Fig. 5(*c*) and inset] than previously, extending over a 4 μm × 4 μm area. A pronounced hole is observed, as well as the vertical and horizontal symmetrical beam tails [area (1) in the inset of Fig. 5(*c*)], and significant damage in the form of rips in the plateau [area (2)] and large aggregates below the beam position.

For both exposures, the damage area is clearly larger than the beam size. The fact that the beam tails expand 1 μm over the reported beam size (that was given in terms of full width at half-maximum) may contribute to this. However, the significantly different behavior between the two illuminations suggests that an additional phenomenon is also contributing to sample damage over a wider area. X-ray radiation-induced damage to samples is a complex process. Damage can occur through direct interaction of the beam, through thermal effects due to absorption of X-ray photons and through the generation of secondary electrons and radicals, which can propagate through the sample over an area much greater than the one directly exposed to the beam (Weiss & Landauer, 2000). We hypothesize that region (1) in Fig. 5(*c*) showing the beam tail has been damaged directly by the beam, whereas the remaining features spread over a much wider area may be due to different damage mechanisms such as secondary electrons and thermal effects. We have no evidence as to which process is leading to the formation of each feature. We also observe that the presence of the tip and the cantilever in the beam's path can induce greater damage to the sample. This effect has been observed several times and additional measurements are reported in Fig. S1 of the supporting information. We hypothesize that, once the beam crosses the tip, distant less than 1 μm from the sample, the electrons emitted from the tip can reach the sample and consequently increase the damage. Indeed, it has been shown that such electrons can travel over several micrometers in the absence of applied electrical fields (Rodrigues, 2009). An accurate beam-tip alignment is therefore necessary to decrease the damage due to the photoelectrons emitted by the tip.

The radiation damage effect was then investigated by measuring the decrease of intensity of the diffraction spot, once AFM tip and X-ray beam were aligned [Fig. 5(*d*)]. The tip aligned with the beam does not affect the position of the diffraction spot in the reciprocal space. It does affect the beam intensity by a few percent as shown in Fig. 4(*b*). We observed a 10% decrease of intensity after 2 s of exposure time that reaches 65% after 40 s [Fig. 5(*e*)]. The upper part of Fig. S1(*b*) (supporting information) shows the radiation damage effects of a 2 s illumination of a sample region above the tip. Despite the short time exposure and the small decrease of intensity of the diffraction spot, we clearly observe the appearance of 100–120 nm deep holes in the sample. Comparing the holes depth

in Figs. 5(*b*) and 5(*c*) (150 nm) with the holes produced in Fig. S1 (∼100 nm), we observe that the morphological effects of a longer exposure (minutes) are very similar to those observed for a faster (seconds) illumination and the main damage occurs in the very first seconds of the exposure. This happens despite the decrease of intensity of the diffraction spot being limited to 10% after 2 s of illumination. This is in agreement with what is known from diffraction experiments where the damage is expected before the observation of clear changes in the diffraction pattern (Garman, 2010). The effect of beam damage to the sample on the position and shape of the diffraction spot can also be seen in the inset of Fig. 5(*e*). In addition to becoming weaker, the diffraction spot also displaces upwards, particularly after about 10 s of illumination. While the decrease of the intensity is due to a decrease of the material contributing to diffraction as shown by the holes in the AFM images, the displacement of the diffraction spot indicates that the lattice expanded slightly during repeated exposure. In addition, the shape of the spot becomes wider: this is likely due to a decrease of order in the crystal.

4.3. Absence of damage at the millisecond timescale

When acquiring AFM images during a permanent X-ray exposure, we are able to homogeneously irradiate the sample over a predetermined area. Figs. 6(*a*) and 6(*b*) present the results obtained for such an experiment. The AFM was used at a speed of 20 s image^{-1} which is relatively fast for standard AFMs.

Here each sample region receives a lower dose compared with the static exposure since the sample is scanned to acquire AFM images. Indeed, each AFM line was acquired in approximately 150 ms which results in an exposure time of 2.5 ms for each sample area of 250 nm × 250 nm during a single AFM image (line scan size = 15 μm). The sample was irradiated for 200 s and ten AFM images were recorded. This
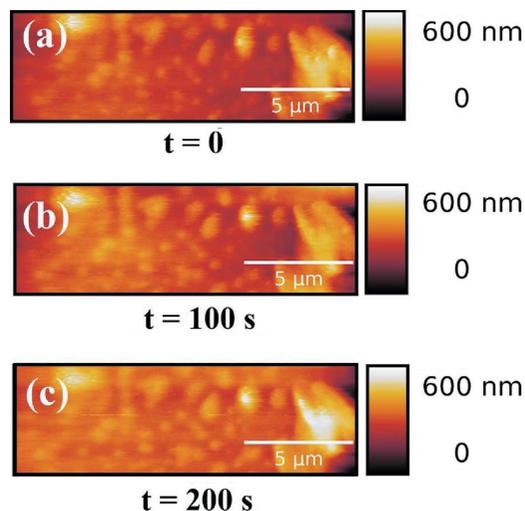
Figure 6
Sequence of fast AFM images acquired while irradiating the sample continuously. In contrast with Fig. 5, no clear formation of holes is observed, suggesting that no damage is present at exposure times of tens of milliseconds. Each image was acquired in 20 s.

intermittent exposure results in a total of 25 ms for each sample area. At such an exposure time, two to three orders of magnitude shorter than the previous experiments, we did not observe any radiation damage (sequence of AFM images in Fig. 6). As a consequence, we can deduce that the main damage is certainly present after the first seconds, as shown in Fig. 5, but it appears at timescales longer than 25 ms. In this way we demonstrate the utility of the *in situ* AFM that can help to define an exposure time which limits the sample damage.

5. Perspectives

In the near future, we will further investigate radiation damage effects at a working energy of 15 keV. At ID13, this energy will provide a higher flux ($\sim 10^{10}$ photons s^{-1}), a smaller beam (~ 150 nm $\times$ 150 nm) and thus a far higher flux density on the sample.

Further applications of this instrument involve the use of the AFM tip as nano-indenter. This will permit the coupling of locally exerted mechanical pressure with variation in the nanoscale structure probed by X-ray scattering. The goal will be to correlate the change of a diffraction pattern as shown in Fig. 5(*d*) with the force applied by the tip. In addition, the high-speed capabilities can be used to investigate any sample dynamics such as thermally induced phase-transitions and electrical or magnetic transitions.

Simultaneous fast acquisition of AFM images and SAXS and WAXS data will be available by synchronizing the X-ray 2D detector with the AFM electronics employing a TTL signal. Then, each pixel of the AFM image will correspond to a single X-ray scattering spectrum.

6. Conclusions

We have developed a custom high-speed X-AFM that can be used *in situ* on synchrotron beamlines, particularly those capable of scanning transmission experiments with highly focused beams. The full range of AFM motorization coupled with the beamline motorization possibilitates the accurate alignment of the AFM tip, X-ray nanobeam and desired sample nanostructures. We have demonstrated that this instrument can be used to monitor the effects of the X-ray beam on the sample morphology. Localized radiation damage was observed as holes created in the sample, as well as the deposition of large aggregates nearby the exposed region. Such effects occurred at a timescale of seconds and minutes. In addition, fast AFM imaging revealed that no damage appeared at a timescale of milliseconds. This instrument also allows the correlation of local molecular structure, determined by X-ray diffraction measurements with the morphology studied by HS-AFM.

7. Access to the instrument

Access to the high-speed X-AFM for beamlines is open to ESRF users. We encourage the users to contact the Surface Science Laboratory and ID13 staff members to discuss possible experiments and proposals involving this instrument. We have improved the instrument to feature high-speed imaging also in a liquid environment, as seen in Fig. S3 of the supporting information.

References

Alizadeh, E., Orlando, T. & Sanche, L. (2015). *Annu. Rev. Phys. Chem.* **66**, 379–398.

Ando, T., Uchihashi, T. & Scheuring, S. (2014). *Chem. Rev.* **114**, 3120–3188.

Brenner, D., Doll, R., Goodhead, D., Hall, E., Land, C., Little, J., Lubin, J., Preston, D., Preston, J., Puskin, J., Ron, E., Sachs, R., Samet, J., Setlow, R. & Zaider, M. (2003). *Proc. Natl Acad. Sci.* **100**, 13761–13766.

Costa, L., Rodrigues, M. S., Benseny-Cases, N., Mayeux, V., Chevrier, J. & Comin, F. (2014). *PLoS One*, **9**, e101687.

Fantner, G., Schitter, G., Kindt, J., Ivanov, T., Ivanova, K., Patel, R., Andersen, N., Adams, J., Thurner, P., Rangelowb, I. & Hansma, P. (2006). *Ultramicroscopy*, **106**, 881–887.

Forrest, S. R. (2004). *Nature (London)*, **428**, 911–918.

Garman, E. F. (2010). *Acta Cryst.* D**66**, 339–351.

Gimzewski, J., Berndt, R. & Schlittler, R. (1992). *Ultramicroscopy*, **42–44**, 366–370.

Gumí-Audenis, B., Carlà, F., Vitorino, M. V., Panzarella, A., Porcar, L., Boilot, M., Guerber, S., Bernard, P., Rodrigues, M. S., Sanz, F., Giannotti, M. I. & Costa, L. (2015). *J. Synchrotron Rad.* **22**, 1364–1371.

Hoogenboom, B., Frederix, P., Fotiadis, D., Hug, H. & Engel, A. (2008). *Nanotechnology*, **19**, 384019.

Larcheri, S., Rocca, F., Jandard, F., Pailharey, D., Graziola, R., Kuzmin, A. & Purans, J. (2008). *Rev. Sci. Instrum.* **79**, 013702.

Martin, Y., Williams, C. C. & Wickramasinghe, H. K. (2002). *J. Appl. Phys.* **61**, 4723–4729.

Pilet, N., Raabe, J., Stevenson, S. E., Romer, S., Bernard, L., McNeill, C. R., Fink, R. H., Hug, H. J. & Quitmann, C. (2012). *Nanotechnology*, **23**, 475708.

Ren, Z., Mastropietro, F., Davydok, A., Langlais, S., Richard, M.-I., Furter, J.-J., Thomas, O., Dupraz, M., Verdier, M., Beutier, G., Boesecke, P. & Cornelius, T. W. (2014). *J. Synchrotron Rad.* **21**, 1128–1133.

Rodrigues, M. M. S. (2009). PhD thesis, Université Joseph-Fourier, France.

Rodrigues, M. S., Cornelius, T. W., Scheler, T., Mocuta, C., Malachias, A., Magalhães-Paniago, R., Dhez, O., Comin, F., Metzger, T. H. & Chevrier, J. (2009). *J. Appl. Phys.* **106**, 103525.

Rodrigues, M. S., Dhez, O., Denmat, S. L., Chevrier, J., Felici, R. & Comin, F. (2008). *J. Instrum.* **3**, P12004.

Rugar, D., Mamin, H. J. & Guethner, P. (1989). *Appl. Phys. Lett.* **55**, 2588–2590.

Schmid, I., Raabe, J., Sarafimov, B., Quitmann, C., Vranjkovic, S., Pellmont, Y. & Hug, H. J. (2010). *Ultramicroscopy*, **110**, 1267–1272.

Slobodskyy, T., Zozulya, A. V., Tholapi, R., Liefeith, L., Fester, M., Sprung, M. & Hansen, W. (2015). *Rev. Sci. Instrum.* **86**, 065104.

Smit, E. de, Swart, I., Creemer, J., Hoveling, G., Gilles, M. K., Tyliszczak, T., Kooyman, P. J., Zandbergen, H. W., Morin, C., Weckhuysen, B. M. & de Groot, F. M. F. (2008). *Nature (London)*, **456**, 222–225.

Vitorino, M. V., Carpentier, S., Panzarella, A., Rodrigues, M. S. & Costa, L. (2015). *Sci. Rep.* **5**, 7818.

Weiss, J. F. & Landauer, M. R. (2000). *Ann. NY Acad. Sci.* **899**, 44–60.